ADVANCED MATERIALS
www.advmat.de

Bandgap Engineering of Melon using Highly Reduced Graphene Oxide for Enhanced Photoelectrochemical Hydrogen Evolution

Muhammad Ashraf, Roshan Ali, Ibrahim Khan, Nisar Ullah, Muhammad Sohail Ahmad, Tetsuya Kida, Sanghyuk Wooh, Wolfgang Tremel, Udo Schwingenschlögl,* and Muhammad Nawaz Tahir**

The uncondensed form of polymeric carbon nitrides (PCN), generally known as melon, is a stacked 2D structure of poly(aminoimino)heptazine. Melon is used as a photocatalyst in solar energy conversion applications, but suffers from poor photoconversion efficiency due to weak optical absorption in the visible spectrum, high activation energy, and inefficient separation of photoexcited charge carriers. Experimental and theoretical studies are reported to engineer the bandgap of melon with highly reduced graphene oxide (HRG). Three HRG@melon nanocomposites with different HRG:melon ratios (0.5%, 1%, and 2%) are prepared. The 1% HRG@melon nanocomposite shows higher photocurrent density (71 µA cm^{-2}) than melon (24 µA cm^{-2}) in alkaline conditions. The addition of a hole scavenger further increases the photocurrent density to 630 µA cm^{-2} relative to the reversible hydrogen electrode (RHE). These experimental results are validated by calculations using density functional theory (DFT), which revealed that HRG results in a significant charge redistribution and an improved photocatalytic hydrogen evolution reaction (HER).

1. Introduction

In times of climate change, renewable energy sources are being extensively studied in order to address the problems of global energy supply and environmental sustainability.[1] Among the renewable energies, H_2 fuel (green hydrogen), produced from water with solar energy, is preferred because of its natural occurrence and ecological compatibility.[2–4] This requires the development of efficient, environmentally friendly, and sustainable technologies for the generation of green H_2 fuel.[2–5] To this end, photocatalytic,[6,7] photoelectrochemical,[1,8] and photoreforming generation of green H_2 fuel by water splitting with solar energy are being investigated.[9–12] One of the most important research areas for these technologies is the synthesis of photocatalysts that can: (i)

M. Ashraf, N. Ullah, M. N. Tahir
Chemistry Department
King Fahd University of Petroleum & Minerals
Dharan 31261, Kingdom of Saudi Arabia
E-mail: muhammad.tahir@kfupm.edu.sa

R. Ali, U. Schwingenschlögl
Physical Science and Engineering Division (PSE)
King Abdullah University of Science and Technology (KAUST)
Thuwal 23955–6900, Saudi Arabia
E-mail: udo.schwingenschlogl@kaust.edu.sa

I. Khan, S. Wooh
School of Chemical Engineering and Materials Science
Chung-Ang University
84 Heukseok-ro, Dongjak-gu, Seoul 06974, Republic of Korea

M. S. Ahmad, T. Kida
International Research Organization for Advanced Science and Technology
Kumamoto University
2-39-1 Kurokami, Kumamoto 860-8555, Japan

M. S. Ahmad, T. Kida
Institute of Industrial Nanomaterials
Kumamoto University
2-39-1 Kurokami, Kumamoto 860-8555, Japan

T. Kida
Department of Advanced Science and Technology
Kumamoto University
2-39-1 Kurokami, Chuo-ku, Kumamoto 860–8555, Japan

W. Tremel
Chemistry Department
Johannes Gutenberg-University
Duesbergweg 10–14, D–55128 Mainz, Germany
E-mail: tremel@uni-mainz.de

M. N. Tahir
Interdisciplinary Research Center for Hydrogen and Energy Storage
King Fahd University of Petroleum & Minerals
Dhahran 31261, Saudi Arabia

The ORCID identification number(s) for the author(s) of this article can be found under https://doi.org/10.1002/adma.202301342

DOI: 10.1002/adma.202301342

make optimal use of the solar spectrum (especially in the visible range of sunlight), (ii) are chemically stable, (iii) inexpensive, and (iv) efficiently separate photoexcited charge carriers.[2,13,14] Transition metal oxides/chalcogenides in combination with noble metals are usually the photocatalysts of choice.[15,16] Major disadvantages that prevent commercialization are the lack of chemical stability under working conditions, the insufficient absorption of sunlight in the visible spectral range, the high demand for precious metals such as platinum, and the associated costs.[16] For practical implementation, metal-free photocatalysts would be much more favorable, particularly carbonaceous materials, as they are naturally abundant, inexpensive, environmentally friendly, and chemically and mechanically stable.[17] Carbon nitride polymers and reduced graphene oxide are utilized in various photocatalytic applications.[18–25] Their optoelectronic properties can be influenced by "proper" synthesis. Moreover, they are affordable and available in nature in sufficient quantities, and they are chemically stable under different pH conditions.[26] Graphitic carbon nitride (g-C_3N_4) was explored for a variety of photocatalytic applications. Melon, an uncondensed form of g-C_3N_4, attracted attention recently.[27–29] It has been used as a precursor for the synthesis of graphitic carbon nitride (g-C_3N_4) since its discovery by Berzelius in the 1830s.[30] It also comprises tri-s-triazine subunits linked through a planar tertiary amino group with a layered structure.[13,31] It resembles g-C_3N_4 in terms of its composition and backbone,[32,33] but differs from g-C_3N_4 by having terminal –NH_2 groups (Scheme S1, Supporting Information). NH_2 groups at the surface can improve the physicochemical properties such as solubility, stability of hole states, and localization of excitons within each heptazine unit of melon.[34] Therefore, melon may be a better choice than g-C_3N_4, for photocatalytic applications such as water splitting. In addition, the NH_2 groups on the surface could provide reactive centers for the preparation of composites through covalent tailoring or weak intermolecular interactions with other functional molecules.[34,35]

Frequently, attempts are made to overcome the shortcomings of metal-free carbon nitride photocatalysts by substitution (i.e., "doping") with nonmetals,[28,29,36,37] by copolymerization,[38,39] or with hybrid heterostructures or nanocomposites.[40,41] Nanocomposites with conductive materials are an intriguing option to improve the charge separation efficiency of semiconductors.[42] Graphene oxide, reduced graphene oxide, or doped graphene-based materials are intuitive examples due to their inherent electronic properties and structural compatibilities.[43,44] As an example, Dai et al. showed that the inclusion of graphene oxide into carbon nitride films resulted in an enhanced photocurrent and photocatalytic efficiency.[45] They proposed the enhancement to be due to better charge separation. In other reports, the inclusion of graphene oxide with g-C_3N_4 led to better efficiencies for the reduction of carbon dioxide to methane[46,47] in the oxygen evolution reaction (OER),[48] for hydrogen generation[49] and pollutant degradation.[50]

Considering these criteria and melon´s structural and functional characteristics, we explored the use of melon in combination with HRG in photoelectrochemical water splitting. We performed experimental PEC studies and verified the mechanism using advanced computational methods to determine whether there is strong electronic coupling at the interface between the optically active metal-free organic semiconductor melon and conductive HRG. We also calculated the role of the remaining O-containing functional groups of HRG. The inclusion of HRG into melon reduced the bandgap of melon and enhanced its optical properties. This explains the significance of including HRG in melon in the charge redistribution at the interface between melon and the HRG sheets. In addition, we tested the role of the amount of HRG by preparing HRG@melon nanocomposites with different HRG/melon ratios and tested the photoelectrochemical water splitting in HER reactions.

2. Synthesis and Properties of HRG@melon

The oxidation of graphite to graphene oxide (GO) followed by reduction to highly reduced graphene oxide (HRG) (Scheme S2, Supporting Information) was monitored by X-ray diffraction (XRD) and Raman spectroscopy. The diffractogram for GO showed a reflection at a lower Bragg angle $2\theta = 12.5°$ (Figure S1a, Supporting Information, blue line). After reduction to HRG, it appeared as a broad reflection between $2\theta = 20°$ and 30°, centered at 25°. This indicates a removal of the O-containing functional groups (**Figure 1**a, black line). The X-ray diffractogram (Figure 1a, red line) of as-synthesized melon shows two reflections $\approx 2\theta =$ 12.32° and 27.45°, respectively.[51] The weak reflection at $2\theta =$ 12.32° corresponds to the (100) plane related to the tri-s-triazine units, and the reflection centered at $2\theta = 27.45°$ corresponds to the (002) plane associated with the aromatic segments.[51] The X-ray diffractogram of the 1% HRG@melon nanocomposite showed a very similar pattern as that of pristine melon and its reported counterpart as it constitutes the major portion of the composite.[45,52,53]

The Raman spectrum of as-synthesized HRG (Figure 1b, black line) shows two well-defined bands centered at 1345 cm^{-1} (D band) and 1585 cm^{-1} (G band). There were significant variations in the intensity ratio for the D and G bands of HRG during the oxidation and reduction steps (Figure S1b, Supporting Information). The Raman spectra of HRG showed a higher intensity ratio of the D/G bands. This indicates that the reduction process increases the average size of the sp^2 domains after the removal of the O-containing functional groups.[54] Raman spectra of pristine melon (Figure 1b, red line) showed a very broad band between 1100 cm^{-1} and 2200 cm^{-1} due to its strong fluorescent background. The broadened D band at 1345 cm^{-1} in the case of the HRG@melon nanocomposite (Figure 1b, blue line) originates from multiple overlapping bands like the D band of graphene, the C–N vibration mode at 1285 cm^{-1}, and the C=N vibration mode of melon at 1400 cm^{-1}. The broadened G band at 1585 cm^{-1} arises from the overlap of the G bands of graphene and melon.

The structure of melon was further confirmed by solid-state ^{13}C and ^{15}N NMR spectra.[55] The ^{13}C cross polarization-magic angle spinning (CP-MAS) spectrum of melon (Figure 1c) showed two sharp signals with peak maxima at $\delta = 166$ and 157 ppm. The low-field signal at $\delta = 166$ ppm was assigned to the carbon atoms adjacent to the amino groups, and the high-field signal at $\delta = 157$ ppm corresponds to the CN_3 moieties in the heptazine ring. For the assignment, the contact time was set to 10 ms (τ_c). The high-resolution ^{15}N CP-MAS spectrum of melon (Figure 1d) showed similarities with the spectra of semicrystalline rather than amorphous materials.[55] A consistent signal was assigned

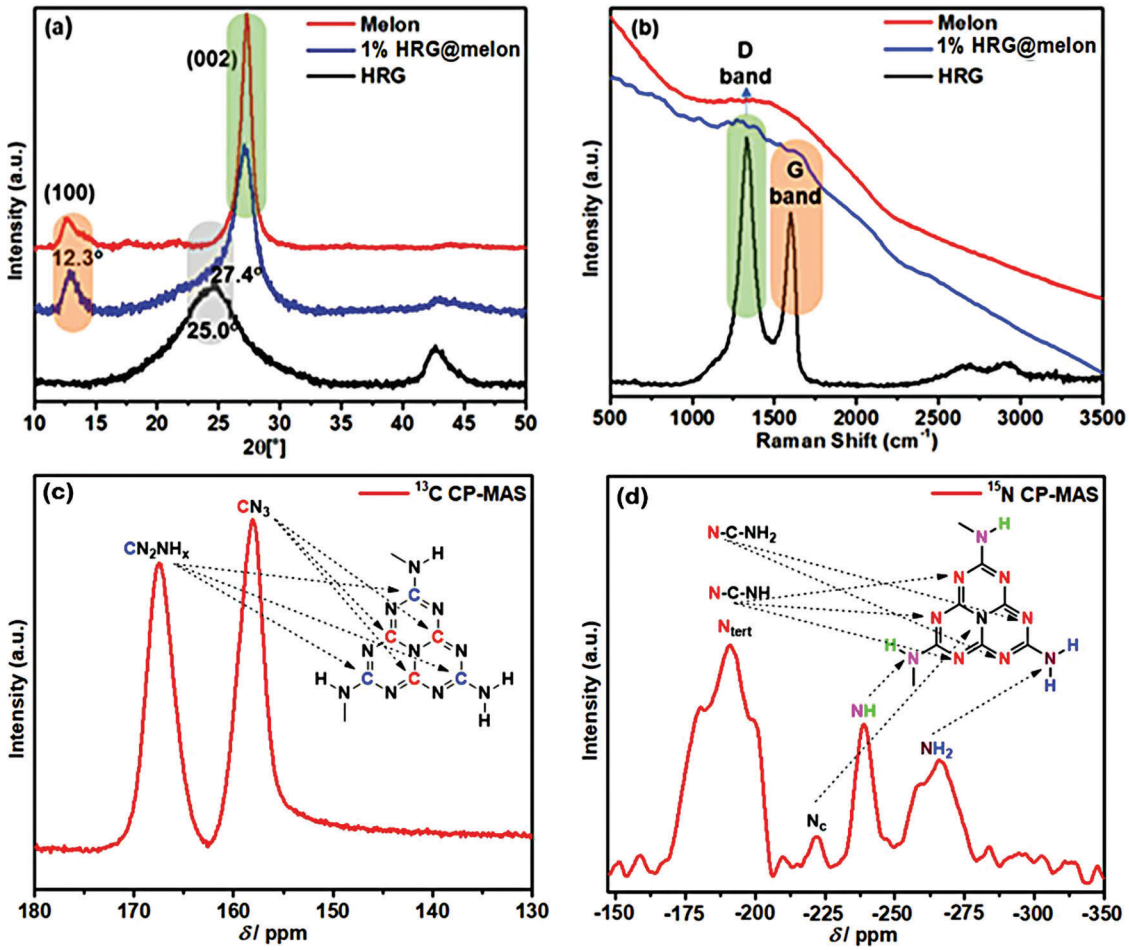

Figure 1. a) XRD pure HRG, pure melon, and the 1% HRG@melon nanocomposite, b) Raman of HRG, pure melon, and the 1% HRG@melon nanocomposite. c) ^{13}C CP-MAS spectra and d) ^{15}N CP-MAS spectra of melon.

through a cross-polarization with polarization inversion (CPPI) experiment using the time dependence of the polarization inversion dynamics of non-equivalent ^{15}N nuclei. The distinguished signals (Figure 1d) contain a broad intense signal from $\delta = -171$ to -205 ppm due to a continuous slow reduction in polarization confirming the presence of tertiary N atoms (N_{tert}). The resonance at $\delta \approx -224$ ppm showing a moderate intensity loss can be ascribed to the central N atom. The signals at $\delta = -245$ and -267 ppm indicate a covalently bonded, proton-induced two-step polarization process. The intensity between the dipolar and spin diffusion regime cross-over according to $[2/(n + 1)] - 1$ ($n = 0$, 1, 2) confirms the variation among the NH (cross-over at 0) and NH_2 (cross-over at $-1/3$) ^{15}N nuclei. The presence of NH and NH_2 groups in the ^{15}N CP-MAS spectrum of melon is in harmony with a partially condensed network structure. The nature of the building blocks can be determined from the isolated intense signal at $\delta = -224$ ppm in the ^{15}N CP-MAS spectrum. The resonance of N_{tert} is indicative of the central N atom (N_c) of the heptazine core.[55,56] The ^{15}N CP-MAS spectrum supports the heptazine-based nature of melon.

The lamellar structure of HRG and 1% HRG@melon was confirmed using scanning electron microscopy (SEM) and transmission electron microscopy (TEM). The SEM and TEM microscopy images of HRG, melon, and the HRG@melon nanocomposites are shown in **Figure 2** and Figure S2 (Supporting Information), respectively. The SEM image of as-synthesized HRG (Figure S2a, Supporting Information) shows a layered structure. This was also confirmed by TEM (Figure 2a). The TEM image (Figure 2a) shows many crumpled and curved layered nanostructures of HRG due to the strong van der Waals interlayer interaction between the sheets. Melon also shows stacked lamellar structures (Figure S2b, Supporting Information). The TEM image of the 1% HRG@melon nanocomposite (Figure 2b) exhibits 2D sheets with well-oriented lamellae of melon stacked with HRG.

The composites were prepared by thoroughly mixing presynthesized HRG and melon by ultrasonication. The 2D characteristic of the two components leads to strong π–π interactions in the basal plane and further intermolecular forces, which explains why specific imaging techniques such as TEM show a high degree of homogeneity.

The 2D morphology and thickness of the HRG sheets and the 1% HRG@melon nanocomposite were confirmed by atomic force microscopy (AFM, tapping mode, Figure 2c–f). The average height profile of HRG (Figure 22) was ≈1.1 nm, which confirms the atomically thin nature of the HRG layer. The thickness of the

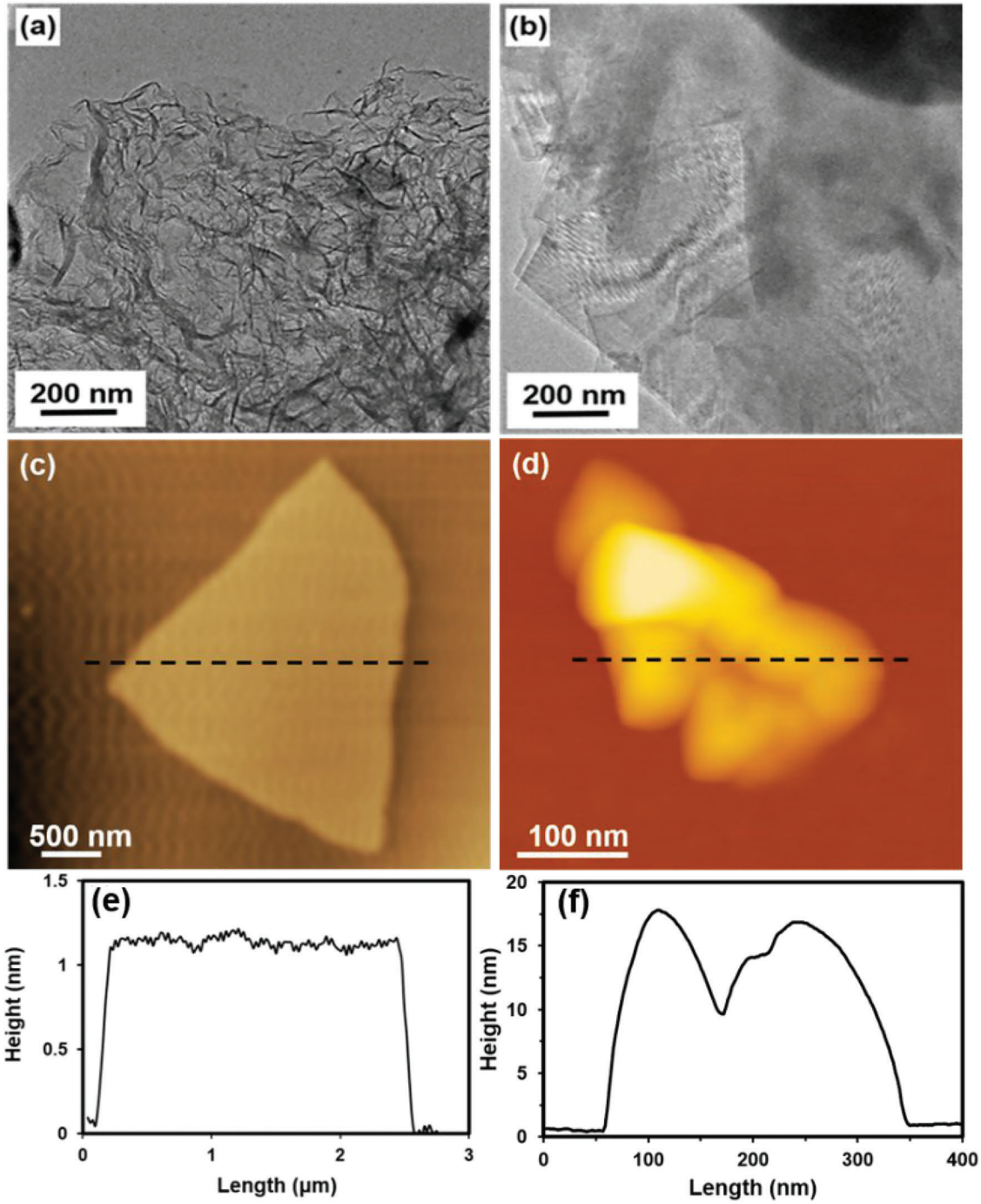

Figure 2. a,b) TEM images of HRG showing the 2D layers (a) and 1% HRG@melon nanocomposite (b) and c,d) tapping-mode AFM images of HRG and 1% HRG@melon nanocomposite. e) Height profile image corresponding to the HRG sheet shown in (c), and f) height profile image of 1% HRG@melon nanocomposite shown in (d). The height profiles (e) and (f) confirm the atomically thick nature of the HRG sheet and also indicate the self-assembly of HRG and melon.

1% HRG@melon nanocomposite was confirmed by measuring the height profile on the AFM image, which showed ≈16.8 nm height (Figure 2f). This suggests an assembly of 2D melon sheets and HRG.

The EDX analysis of the field-emission scanning electron microscopy SEM (FE-SEM) for the 1% HRG@melon nanocomposite confirms the presence of C and N as major elements (Figure S2d, Supporting Information) in the nanocomposite. The empirical formula calculated from the elemental analysis (Table S1, Supporting Information) is $C_{2.98}$:$N_{4.39}$:$H_{3.33}$. Although the H content is higher than expected with this formula, this phenomenon is well documented in the literature.[1,57,60]

The chemical structure of HRG, melon, and the 1% HRG@melon nanocomposite was analyzed using Fourier-transform infrared spectroscopy (FTIR) and X-ray photoelectron spectroscopy (XPS). The FTIR spectrum of HRG (Figure S3a, Supporting Information, black line) shows only weak peaks ≈1704 and 1611 cm^{-1} and a broad peak ≈700 cm^{-1}. The peaks ≈1704 cm^{-1} and 1611 cm^{-1} are related to the stretching modes of the C=O and C=C moieties, whereas that at 700 cm^{-1} is due to out-of-plane deformations of the C–H moiety. This shows the reduction of most O-containing functionalities. Melon and the 1% HRG@melon nanocomposite (Figure S3a, Supporting Information, red and blue lines) show peaks between 1200 and 1600 cm^{-1}. These are due to the stretching of the C–N moiety in the heterocycles. A weak broad peak between 3100 and 3350 cm^{-1} (Figure S3a, Supporting Information, red line) is assigned to the $–NH_2$ moiety of melon. A weak sharp peak at 810 cm^{-1} is attributed to the stretching of the triazine moiety of melon. Figure S3b (Supporting Information) shows the survey spectra of HRG, melon, and the 1% HRG@melon nanocomposites. They indicate the presence of C and N for melon (Figure S3b, Supporting Information, red line), C and O for HRG (Figure S3b, Supporting Information, black line), and C, N, and O for the 1% HRG@melon nanocomposite (Figure S3b, Supporting Information, blue line).

The high-resolution C 1s spectrum (**Figure 3**a) for HRG supports the reduction because the peak centered at 284.5 eV corresponds to sp^2 carbon, i.e., the C=C moiety. The other signals associated with the C 1s signal, which are due to the C–O or C=O moieties and centered at 285.7 and 288.3 eV, respectively, are greatly reduced. This confirms that the structure of HRG contains mostly C atoms of an sp^2 skeleton. Deconvolution by Gaussian curve fitting for the O 1s spectrum (Figure 3b) points out the presence of three chemically different O species with O 1s binding energies centered at 530.7, 533, and 535 eV. The intense peak at ≈533 eV is attributed to the C–O moiety, while the peaks at 530.7 and 535 eV are attributed to the C=O and O–H– moieties, respectively. The high-resolution XPS spectrum of melon shows two C 1s peaks centered at 284.6 and 288.6 eV (Figure 3c). The peak at 284.6 eV is assigned to C 1s of the C=N moiety inside the aromatic ring and that at 288.6 eV to the heteropolar C–N moiety, as reported previously.[26,58,59] The high-resolution XPS spectrum in the N 1s regime of melon shows four peaks upon deconvolution (Figure 3d). They are centered at 398.7, 399.6, 400.4, and 401.4 eV and correspond to the pyridinic N atoms, the $–NH_2$ and –NH– moieties, and to the quaternary N atoms, respectively. The presence of the $–NH_2$ moiety shows the uncondensed nature of melon. The high-resolution XPS spectrum in the C 1s regime of the 1% HRG@melon nanocomposite (Figure 3e) shows similar binding energies as that of melon. The asymmetry of the peaks indicates the presence of chemically different C species, but it is difficult to quantify them due to the overlap in the binding energies of the C=C moiety in HRG and the C=N moiety in melon. This overlap explains the high intensity in the graphitic carbon region. The high-resolution XPS spectrum in the N 1s regime of the 1% HRG@melon nanocomposite (Figure 3f) shows similar binding energies as that of melon. However, the peaks are broadened due to the inclusion of HRG.

3. Optical and Electronic Properties

The optical properties and the bandgaps of pristine HRG, melon, and the 1% HRG@melon nanocomposite were determined by UV-visible diffuse reflectance spectroscopy. **Figure 4**a shows the diffuse reflectance absorption spectra of HRG, melon, and the 1% HRG@melon nanocomposite. HRG shows a very weak absorption, mostly in the UV region (Figure 4a, black line). Melon shows a broad absorption in the UV-visible region with an absorption edge at ≈480 nm (Figure 4a, red line). However, with 1% HRG@melon, the absorption edge is redshifted (≈520 nm) to the visible region (Figure 4a, blue line).[50] The bandgap energies were estimated from the Kubelka–Munk functions. The bandgap energies for melon and the 1% HRG@melon nanocomposite are 2.6 and 2.4 eV, respectively (Figure 4b). The enhancement of the visible light utilization and narrowing of the bandgap in the nanocomposite can be attributed to the contact of the HRG nanosheets with the melon lamella which results in an charge redistribution at the interface between HRG and melon. The valence band (VB) and conduction band (CB) potentials of pristine melon, HRG, and the HRG@melon nanocomposite were calculated using the empirical equations (1–3):

$$E_{CB} = X - E_e - \frac{1}{2}E_g \quad (1)$$

$$X = \left[X(C)^a \times X(N)^b \times X(O)^c\right]^{1/(a+b+c)} \quad (2)$$

$$E_{VB} = E_{CB} + E_g \quad (3)$$

where E_{CB} and E_{VB} are the conduction and VB energies and X stands for the geometric average of the absolute electronegativities of the corresponding atoms of a semiconductor calculated from Equation (2). The superscripts a, b, and c represent the numbers of atoms of C, N, and O in the chemical formula of the semiconductor, respectively, E_e is the energy of a free electron on the hydrogen scale (4.5 eV), and E_g is the bandgap. By applying the above formulae, the relative positions of E_{CB} and E_{VB} are presented graphically in Figure 4c.

4. Photoelectrochemical Splitting of Water

The photoelectrochemical water splitting performance of the as-fabricated photoelectrodes using melon in combination with different ratios of HRG was measured in a 3-electrode cell under AM 1.5 G illumination. The results are shown in **Figure 5**a. The conductive character of HRG (a zero-bandgap material) facilitates charge transfer in many optoelectronic applications.[42,60–62] As expected, the inclusion of HRG enhanced the photoelectrochemical HER activity by charge redistribution at the interface between HRG and melon (semiconductor nature with bandgap > 2).[63,64] The *I-V* behavior of the as-fabricated melon and HRG@melon photoelectrodes (Figure 5a and Table S2, Supporting Information) under illumination indicates the solar light impact on the photoelectrochemical behavior of the as-fabricated photoelectrodes. Under simulated light exposure, the photoelectrodes show a significant increase in the current density

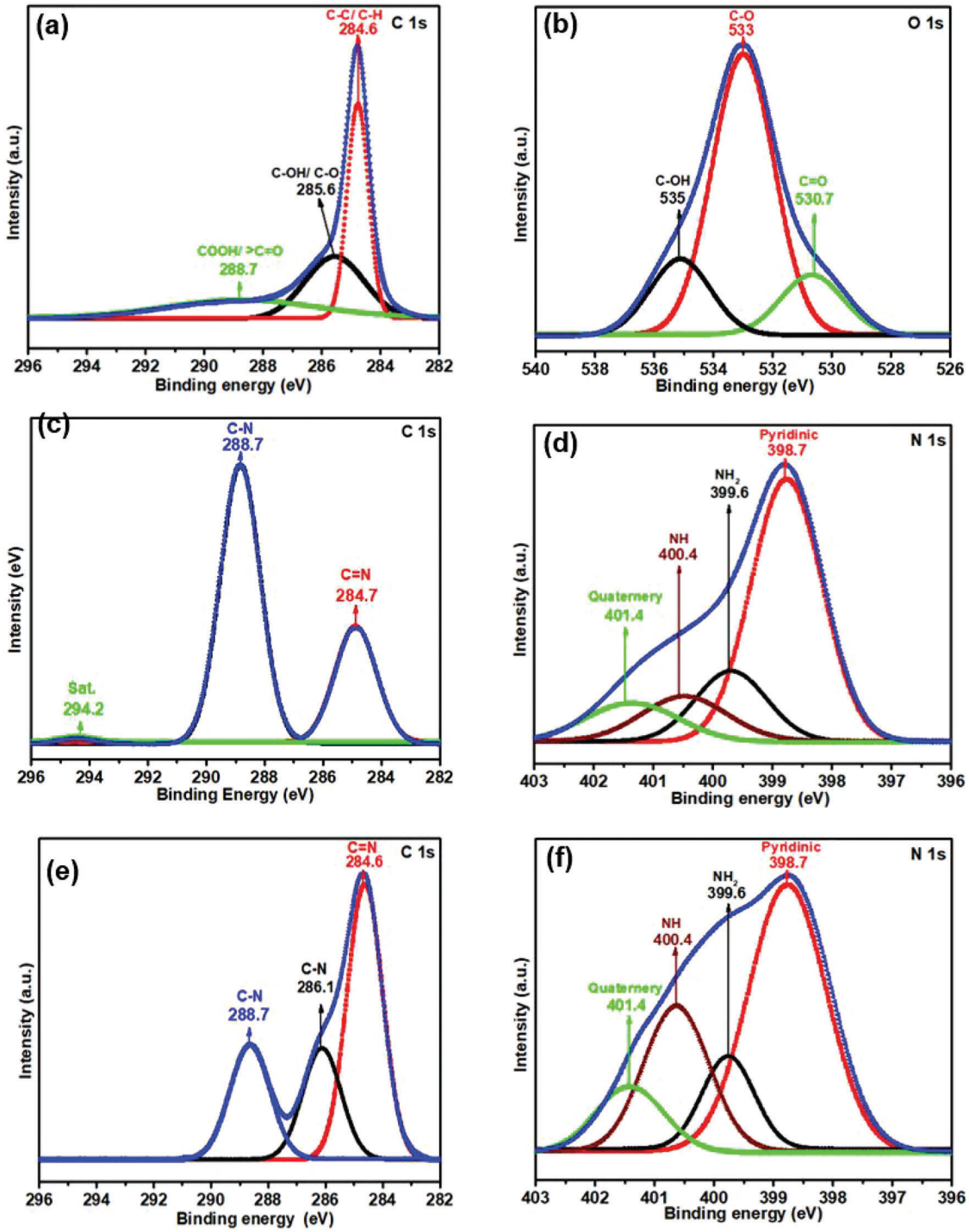

Figure 3. a–f) XPS spectra of HRG C 1s (a), HRG O 1s (b), melon C 1s (c), melon N 1s (d), 1% HRG@melon nanocomposite C 1s (e), and 1% HRG@melon nanocomposite N 1s (f).

compared to dark conditions.[52] We compared the linear sweep voltammograms of the HRG@melon photoelectrodes with different percentages of HRG and melon (Figure 5a and Figure S4, Supporting Information) under continuous AM 1.5 G illumination in 0.1 m KOH aqueous electrolyte containing 10% (volume/volume) triethanolamine. The photoelectrode consisting of only melon shows only a low photocurrent under light with a significant onset potential, i.e., 0.071 mA cm^{-2} at −0.75 V_{RHE}. In contrast, the photoelectrode prepared from the 1% HRG@melon nanocomposite shows the highest photocurrent density of 0.63 mA cm^{-2} at −0.75 V_{RHE}. The other photoelectrodes containing 0.1% and 2% HRG did not show a better

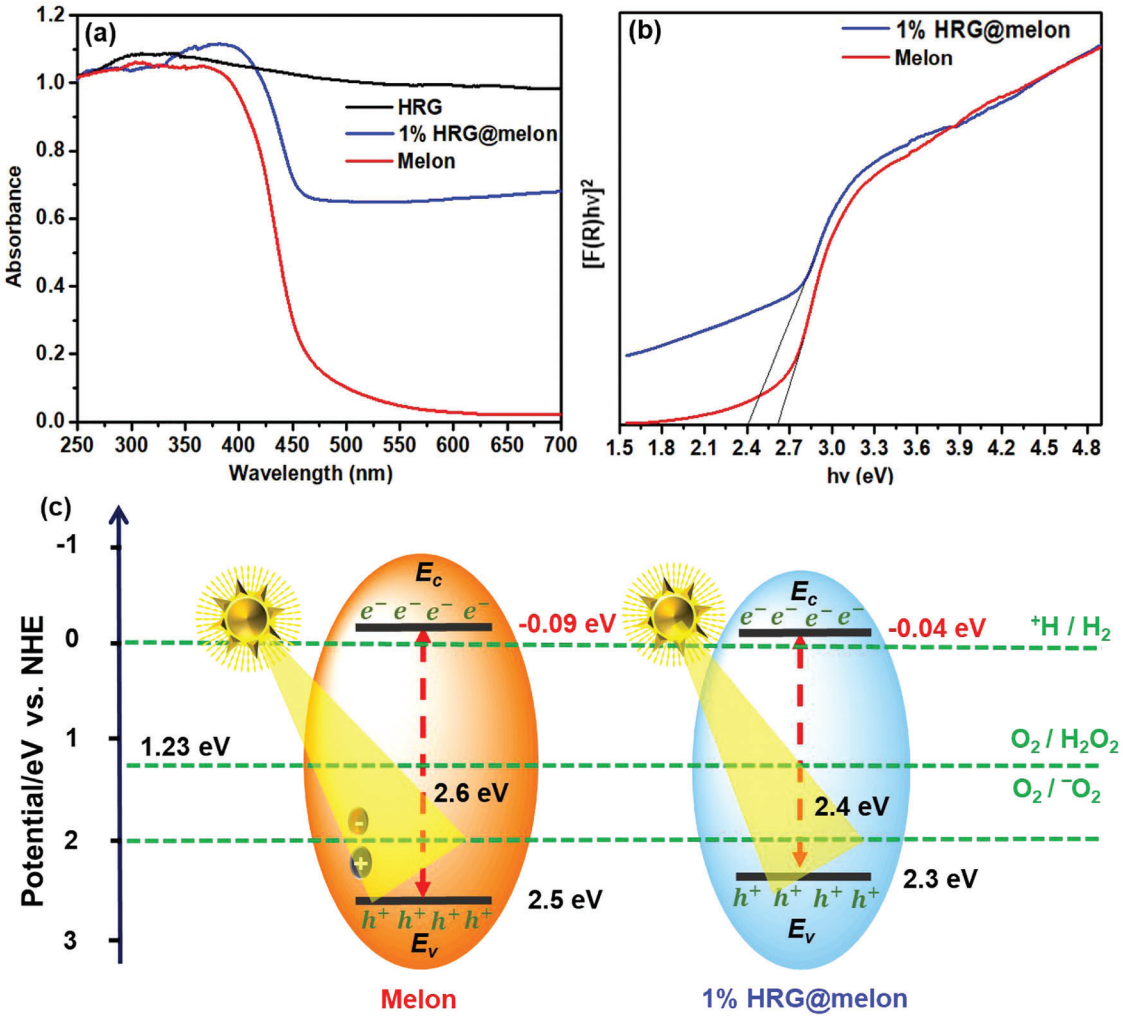

Figure 4. a) UV–visible diffuse absorption spectra of melon, HRG, and the 1% HRG@melon nanocomposite. b) Kubelka–Munk functions vs light energy. c) Scheme of the theoretical optical band positions for melon and the 1% HRG@melon nanocomposite.

photocurrent. For the composite with 0.1% HRG, it could be because the amount of HRG was insufficient for a significant effect, while with 2% HRG, a conventional conductive behavior occurred, resulting in only an insignificant improvement under light exposure. Additionally, the higher amount of HRG (2%) contributes more to the electrochemical behavior of HRG, which dominates the photocatalytic performance at higher concentrations. It provides a feasible pathway for electronic transport from melon.[65] Furthermore, the potential onset value is shifted significantly toward lower cathodic potentials with HRG and improves until 1%, i.e., from −0.71 V_{RHE} (in the case of melon) to −0.24 V_{RHE} at 0.05 mA cm^{-2} for 1% HRG@melon nanocomposite. Thus, the 1% HRG@melon nanocomposite shows the best photoelectrochemical behavior among the three different HRG@melon photoelectrodes.

The photostability of the photoelectrodes in terms of the *I–t* plots was analyzed by chronoamperometry. The chronoamperometric curves (Figure 5b) declined initially slightly due to the possible charge recombination behavior.[66] However, the photocurrent was sustained up to 2000 s with only minimal loss. We also carried out transient photocurrent tests to explore photocurrent stability and recovery (Figure 5c). All samples showed recoverable photocurrent density levels under solar illumination, indicating a typical photocatalyst behavior. As expected, the photocurrent density level is sustained after multiple transient cycles, specifically for 1% HRG@melon.

Electrochemical impedance spectroscopy (EIS) analysis was carried out to understand the effect of HRG on the resistances and the separation efficiency of the charge carriers. The EIS analysis was performed using 0.1 M KOH aqueous solution as an electrolyte under visible light. In the EIS Nyquist plot (Figure 5d), the pristine samples showed larger radii than the 1% HRG@melon nanocomposite. The order of decreasing semicircle radii is melon > HRG > 1% HRG@melon. Upon illumination, the 1% HRG@melon nanocomposite showed a higher charge transfer than melon. The Randles circuit[67] of the 1% HRG@melon nanocomposite is provided as an inset in Figure 5d, where C_{dl}, R_s, W, CPE, and R_{ct} are the double-layer capacitance, electrolytic Ohmic resistance, diffusion resistance, constant phase element, and charge-transfer resistance,

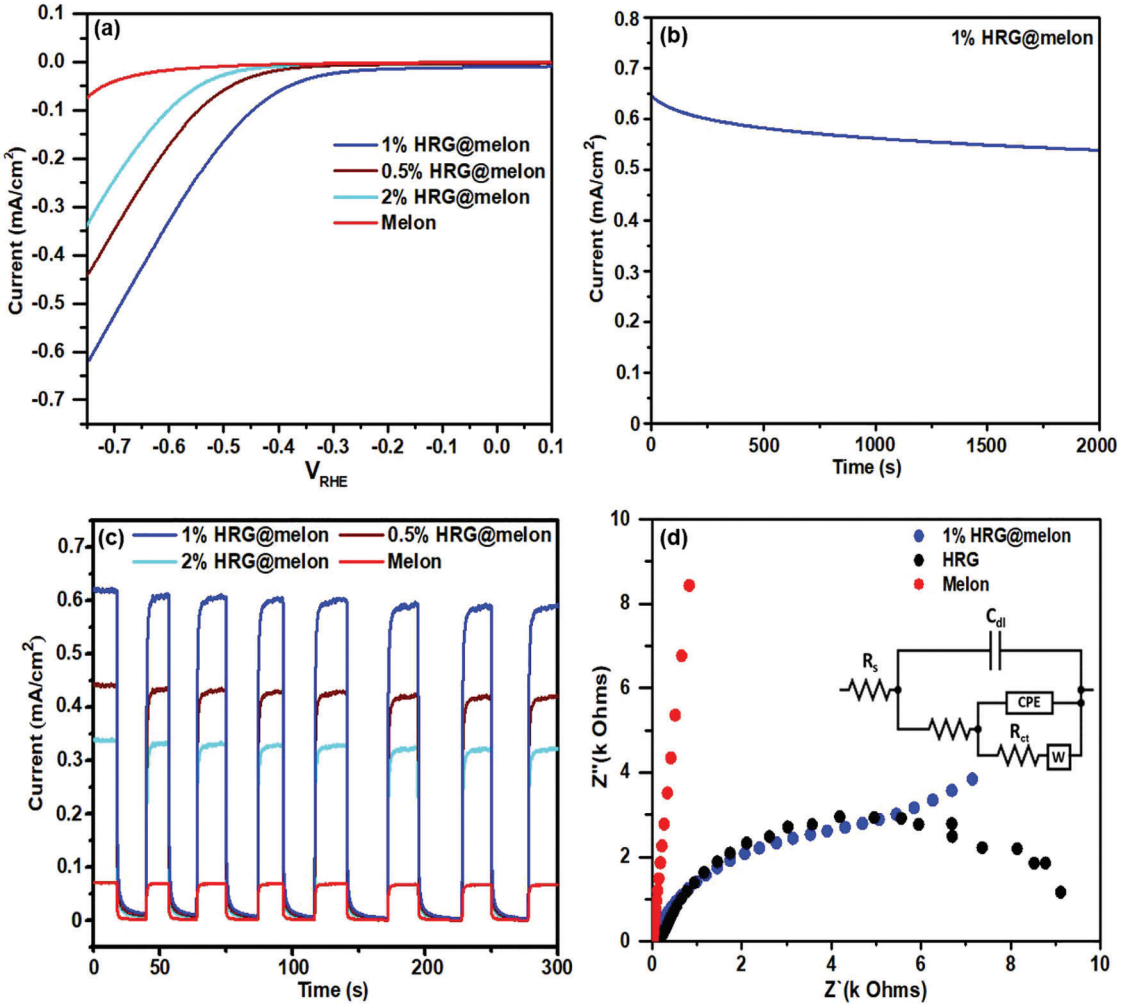

Figure 5. a) Linear sweep voltammograms of pristine melon, and 0.5%, 1%, and 2% HRG@melon nanocomposites in 0.1 M KOH aqueous electrolyte containing 10% (v/v) triethanolamine under visible light irradiation for hydrogen evolution reactions. b) Chronoamperometric curves of the 1% HRG@melon nanocomposite. c) Transient photocurrents of melon and 0.5%, 1%, and 2% HRG@melon nanocomposites in 0.1 M KOH aqueous electrolyte containing 10% (volume/volume) triethanolamine under visible light. d) Photoelectrochemical impedance spectra of melon, HRG, and 1% HRG@melon nanocomposite. The Randles circuit of the 1% HRG@melon nanocomposite is provided as an inset in (d).

respectively. The enhanced activity of HRG@melon in photocatalytic applications results from the fact that:[68] (i) the assembly of HRG and melon reduces the bandgap of melon from 2.6 to 2.4 eV and (ii) the peripheral amino groups of melon enhance the wettability of the photoanodes and improve the kinetics of the HER.

Further elucidation of the mechanism was possible with a Mott–Schottky analysis. **Figure 6** shows that the incorporation of HRG shifted the band position from −0.91 $V_{Ag/AgCl}$ to −0.76 $V_{Ag/AgCl}$. This leads to an enhanced photoelectrochemical HER activity of the 1% HRG@melon photoelectrode at a lower potential than for the melon photoelectrode, which is due to: (i) the high surface area of HRG, (ii) the presence of π-conjugated heptazine moieties of melon, and (iii) the charge redistribution at the interface of HRG and melon. The materials have n-type conductivity as the slopes of the Mott–Schottky plots are positive.

To gain a better mechanistic insight, we performed first-principles calculations (details are given in Supporting Information) to study the coupling between RG and melon. **Figure 7**a shows the crystal structure of the melon (unit cell marked), and Figure 7b,c shows the obtained band structures and projected densities of states, respectively. We find a direct bandgap of 2.6 eV at the Γ-point, which is consistent with our experimental value of 2.6 eV and with previous experimental (2.7 eV) and theoretical (2.6 eV) results.[33] The projected densities of states indicate that the VB edge is dominated by N p states, while the conduction band edge is dominated by hybridized C p and N p states. Melon has a high absorption coefficient in the range of 10^5 cm^{-1} (Figure S5, Supporting Information).

The Gibbs free energy difference (ΔG_{H^*}) can be used to predict the HER activity. The ideal value of zero indicates that H is neither too weakly nor too strongly bound. In the case of melon, we calculate ΔG_{H^*} for 38 N sites and find that the symmetry-equivalent sites 1, 2, 7, 9, 10, 16, 21, 27, 28, 30, 35, and 36 are highly HER active with ΔG_{H^*} = 0.39 eV (Figure S6, Supporting Information). As the addition of 1% HRG enhances the HER

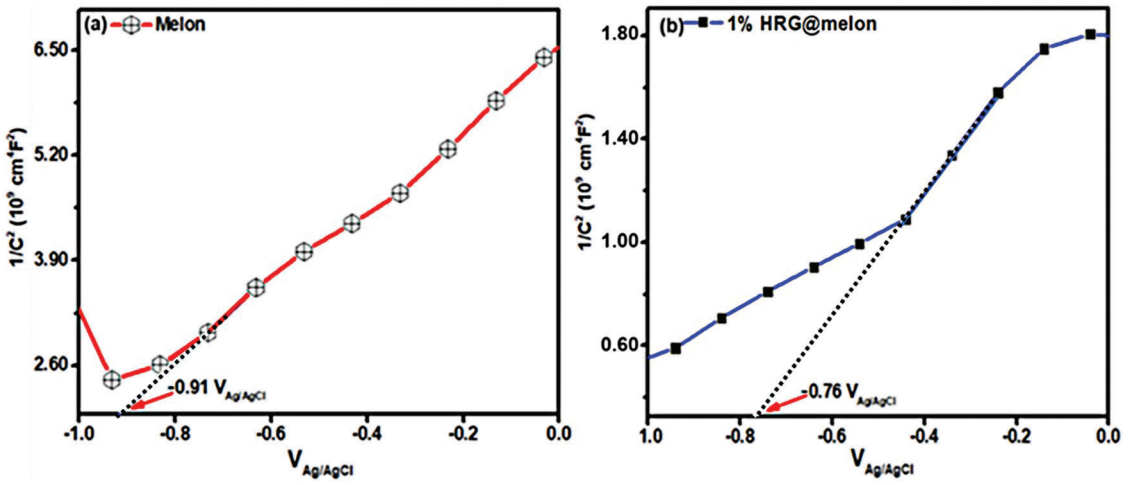

Figure 6. a,b) Mott–Schottky plots indicating the band positions for melon (a) and the 1% HRG@melon nanocomposite (b).

activity of melon experimentally, we add an HRG nano-sheet to our simulation model. Specifically, we place HRG above the void area of the melon (i) or above the heptazine unit of the melon (ii) (Figure S7, Supporting Information). Again we study all 38 N sites with an OH functional group attached to the HRG nano-sheet at two different positions (red circles in Figure S7, Supporting Information). The same sites as before are found to be highly HER active (red values in Table S4, Supporting Information). Among them, site 9 is particularly favorable for high HER activity. Therefore, we consider for this case additionally O, OH, and/or COOH functional groups attached to the HRG nano-sheet (Figure 8a,b). Figure 8c,d and Table S4 (Supporting Information) show that the addition of HRG to melon improves ΔG_{H^*}, which confirms our experimental findings. Next, we study the charge transfer in HRG@melon with attached O, OH, and COOH functional groups when HRG is placed above the void area of the melon and when HRG is placed above the heptazine unit of the melon. Figure 8e–h demonstrates a significant charge redistribution, which may enhance the conductivity.

It is instructive to compare the HRG@melon nanocomposites with other materials from the carbon nitride group that are successful in photochemical hydrogen generation.[33,69–71] As compared to prototypical carbon nitrides such as poly(triazine-imide) (PTI) and poly(heptazine-imide) (PHI), melon has the most appropriate conduction band and therefore exhibits the highest thermodynamic driving force for the HER. However, since the HER does not correlate directly with the positions of the valence and conduction bands, competing factors and/or kinetic

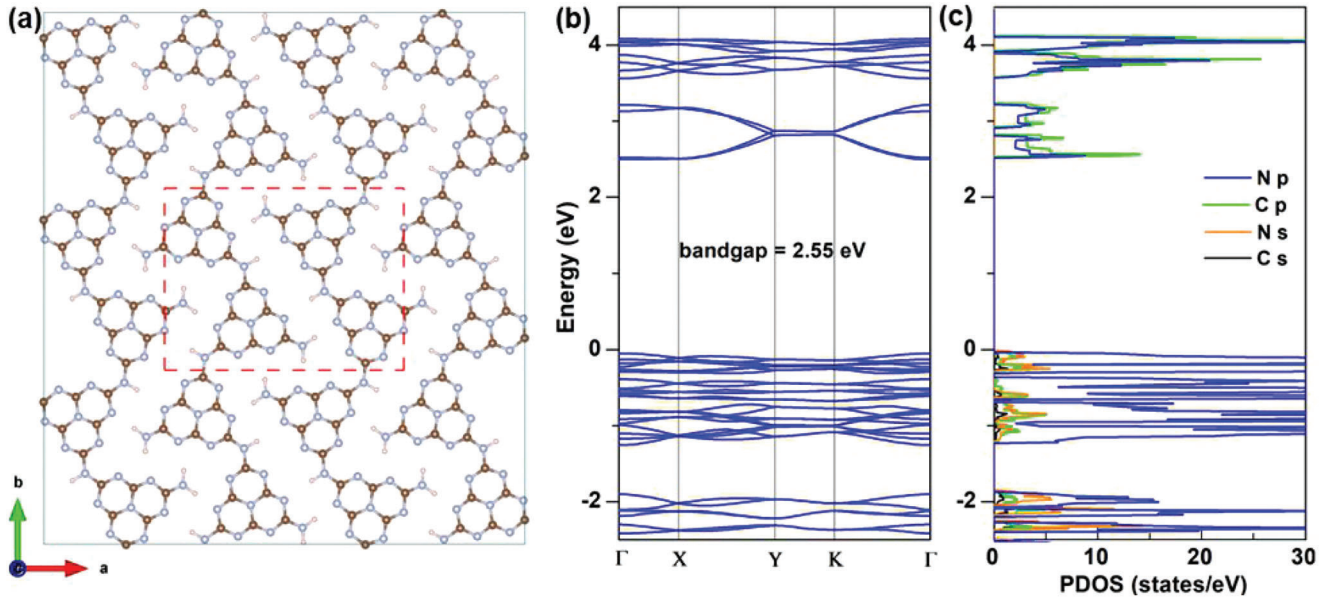

Figure 7. a) Crystal structure of melon with unit cell boundaries. b) Band structure and c) projected densities of states of melon obtained with the Perdew–Burke–Ernzerhof functional.

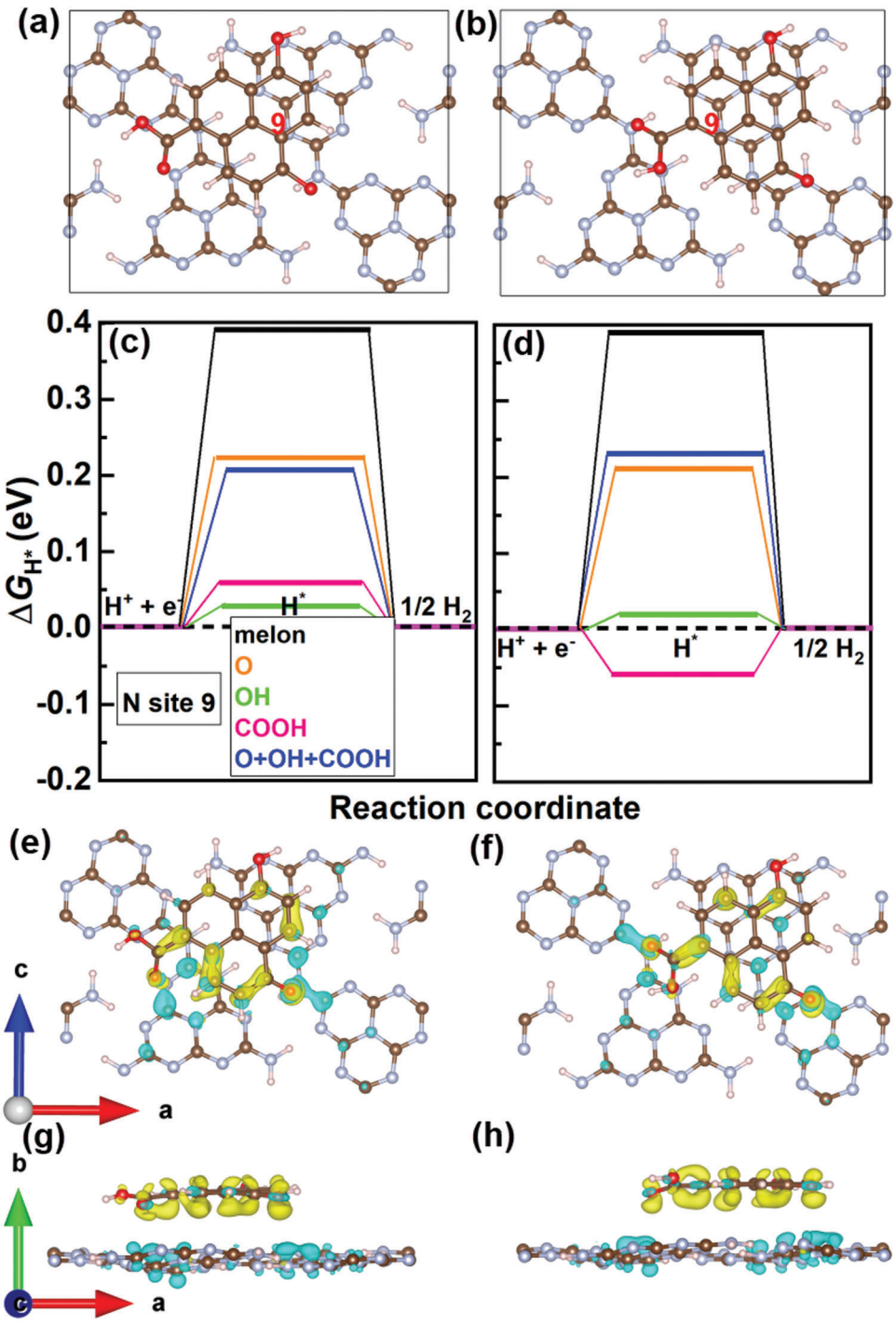

Figure 8. a,b) HRG on melon above the void area of melon (a) and above the heptazine of melon (b). c,d) The obtained values of ΔG_{H^*} for H adsorption at site 9 (favorable for high HER activity), respectively, for HRG with attached O, OH, and/or COOH functional groups. e–h) Charge transfer between HRG and melon in top (e) and side (g) views when HRG is placed above the void area of melon, and in top (f) and side (h) views when HRG is placed above the heptazine of melon. The yellow and cyan colors (iso-value of 0.001 eÅ^{-3}) represent electron accumulation and depletion, respectively.

barriers may be important as well. This point is addressed in the present work by studying HRG@melon nanocomposites. In melon-type materials, small stacking distances and crystallinity enhance the exciton dissociation and charge transport.[72] Higher crystallinity prolongs non-radiative relaxation pathways in PHI-type materials,[73] but is not reflected directly by their HER activity. Structural ordering in layered carbon nitrides leads to higher π-conjugation, which, in turn, decreases the band gap, resulting in enhanced light absorption.[74] The high VB potential of PHI makes photoexcited holes to strong oxidants,[75] which we

also observe for the HRG@melon nanocomposites. In contrast, amorphization of melon disrupts the hydrogen bonding between layers and the removal of dangling amine residues enhances the HER activity.[76] We show here by first-principles calculations that OH and COOH functional groups of the HRG component lead to a redistribution of charge that ultimately lowers the activation energy of the HER, similar to the higher photocatalytic activity of amorphous PTI as compared to that of crystalline PTI.[74] The role of chain ends as catalytic centers in carbon nitrides and thus the usefulness of oligomeric building blocks to enhance the photocatalytic activity was analyzed by transient absorption spectroscopy for exfoliated g-C_3N_4 on bulk g-C_3N_4.[75] A charge is generated by the dissociation of excitons in bulk g-C_3N_4 followed by diffusion-controlled electron transfer into exfoliated g-C_3N_4, which contains active catalytic centers that double the HER activity as compared to bulk g-C_3N_4. A similar function of HRG in the HRG@melon nanocomposites may be envisioned.

5. Conclusion

We have synthesized HRG, melon, and HRG@melon nanocomposites with different HRG:melon ratios. The nanocomposites were tested for photoelectrochemical water splitting. Our experimental data show that the inclusion of 1% HRG enhances the HER activity by approximately one order of magnitude. The findings were corroborated by first-principles calculations. Both experimental and theoretical results indicate that the enhanced HER activity is due to the: (i) high surface area of HRG, (ii) presence of π-conjugated heptazine moieties of melon, and (iii) charge redistribution at the interface of HRG and melon. Moreover, the presence of primary amine groups in melon enhances the wettability of the photoanodes. In addition, we studied the effect of the O-containing functional groups (O, OH, and/or COOH) of HRG on the HER activity. Importantly, the designed photocatalyst (1% HRG@melon nanocomposite) has excellent potential for efficient HER even without the use of expensive metals or metal oxides. The HRG@melon nanocomposites can also be applied as green, cost-effective, and efficient photocatalysts for related applications such as photoreforming, light-induced organic reactions, and solar energy conversion.

Supporting Information

Supporting Information is available from the Wiley Online Library or from the author.

Acknowledgements

The research reported in this publication was supported by funding from King Abdullah University of Science and Technology (R. A. and U. S.) as well as King Fahd University of Petroleum and Minerals (M.A., N.U., and M.N.T.).

Open access funding enabled and organized by Projekt DEAL.

Conflict of Interest

The authors declare no conflict of interest.

Data Availability Statement

Research data are not shared.

Keywords

2D materials, HRG@melon, hydrogen evolution, melon, PEC water splitting

Received: February 11, 2023
Revised: June 30, 2023
Published online:

[1] V. W.-h. Lau, B. V. Lotsch, *Adv. Energy Mater.* **2022**, *12*, 2101078.
[2] H. Ishaq, I. Dincer, *Renewable Sustainable Energy Rev.* **2021**, *135*, 110192.
[3] L. Kong, L. Li, G. Cai, C. Liu, P. Ma, Y. Bian, T. Ma, *Int. J. Hydrogen Energy* **2021**, *46*, 2847.
[4] A. Kovač, M. Paranos, D. Marciuš, *Int. J. Hydrogen Energy* **2021**, *46*, 10016.
[5] K. C. Christoforidis, P. Fornasiero, *ChemCatChem* **2017**, *9*, 1523.
[6] G. Zhang, Z.-A. Lan, X. Wang, *Angew. Chem., Int. Ed.* **2016**, *55*, 15712.
[7] C. F. Fu, X. Wu, J. Yang, *Adv. Mater.* **2018**, *30*, 1802106.
[8] X. Peng, R. M. Kelly, Y. Han, *Biotechnol. Bioeng.* **2018**, *115*, 1624.
[9] T. Uekert, H. Kasap, E. Reisner, *J. Am. Chem. Soc.* **2019**, *141*, 15201.
[10] T. Uekert, M. F. Kuehnel, D. W. Wakerley, E. Reisner, *Energy Environ. Sci.* **2018**, *11*, 2853.
[11] T. Uekert, F. Dorchies, C. M. Pichler, E. Reisner, *Green Chem.* **2020**, *22*, 3262.
[12] M. Ashraf, N. Ullah, I. Khan, W. Tremel, S. Ahmad, M. N. Tahir, *Chem. Rev.* **2023**, *123*, 4443.
[13] H.-H. Wang, L. Xue, C.-L. Yu, Y.-Y. Qian, H. Jiang, *Dyes Pigm.* **2011**, *91*, 350.
[14] T. Takata, K. Domen, *ACS Energy Lett.* **2019**, *4*, 542.
[15] M. Ashraf, I. Khan, M. Usman, A. Khan, S. S. Shah, A. Z. Khan, K. Saeed, M. Yaseen, M. F. Ehsan, M. N. Tahir, N. Ullah, *Chem. Res. Toxicol.* **2020**, *33*, 1292.
[16] Y. Yang, S. Niu, D. Han, T. Liu, G. Wang, Y. Li, *Adv. Energy Mater.* **2017**, *7*, 1700555.
[17] D. Zhang, E. Mitchell, X. Lu, D. Chu, L. Shang, T. Zhang, R. Amal, Z. Han, *Mater. Today* **2023**, *63*, 339.
[18] J. Wang, J. Hao, D. Liu, S. Qin, D. Portehault, Y. Li, Y. Chen, W. Lei, *ACS Energy Lett.* **2017**, *2*, 306.
[19] R. Kuriki, K. Sekizawa, O. Ishitani, K. Maeda, *Angew. Chem., Int. Ed.* **2015**, *54*, 2406.
[20] G. Gao, Y. Jiao, E. R. Waclawik, A. Du, *J. Am. Chem. Soc.* **2016**, *138*, 6292.
[21] H. Xu, J. Yi, X. She, Q. Liu, L. Song, S. Chen, Y. Yang, Y. Song, R. Vajtai, J. Lou, H. Li, S. Yuan, J. Wu, P. M. Ajayan, *Appl. Catal., B* **2018**, *220*, 379.
[22] H. Ou, P. Yang, L. Lin, M. Anpo, X. Wang, *Angew. Chem. Int. Ed.* **2017**, *56*, 10905.
[23] M. S. Reza, N. B. H. Ahmad, S. Afroze, J. Taweekun, M. Sharifpur, A. K. Azad, *Chem. Eng. Technol.* **2023**, *46*, 420.
[24] S. Cao, J. Yu, *J. Photochem. Photobiol., C* **2016**, *27*, 72.
[25] C. M. Aitchison, S. Gonzalez-Carrero, S. Yao, M. Benkert, Z. Ding, N. P. Young, B. Willner, F. Moruzzi, Y. Lin, J. Tian, P. D. Nellist, J. R. Durrant, I. McCulloch, *Adv. Mater.* **2023**, https://doi.org/10.1002/adma.202300037.
[26] J. Liang, X. Yang, Y. Wang, P. He, H. Fu, Y. Zhao, Q. Zou, X. An, *J. Mater. Chem. A* **2021**, *9*, 12898.

[27] C. Jiang, H. An, G. Dong, J. Feng, M. Zhang, Y. Ren, J. Ma, *Chem. Eng. J.* **2022**, *428*, 131054.
[28] H. Y. Yuan, J. Y. Bai, B. Xu, X. Y. Li, S. Y. Xiao, P. F. Liu, X. L. Wang, H. G. Yang, *Chem. Commun.* **2021**, *57*, 3042.
[29] X. Bai, M. Li, J. Li, X. Rao, S. Zheng, Y. Zhang, *ACS Appl. Energy Mater.* **2021**, *4*, 14390.
[30] Y. Wang, X. Wang, M. Antonietti, *Angew. Chem., Int. Ed.* **2012**, *51*, 68.
[31] E. Alwin, W. Nowicki, R. Wojcieszak, M. Zieliński, M. Pietrowski, *Dalton Trans* **2020**, *49*, 12805.
[32] T. P. Ang, Y. M. Chan, *J. Phys. Chem. C* **2011**, *115*, 15965.
[33] X. Wang, K. Maeda, A. Thomas, K. Takanabe, G. Xin, J. M. Carlsson, K. Domen, M. Antonietti, *Nat. Mater.* **2009**, *8*, 76.
[34] J. E. Ellis, D. C. Sorescu, S. C. Burkert, D. L. White, A. Star, *ACS Appl. Mater. Interfaces* **2017**, *9*, 27142.
[35] S. T. A. G. Melissen, T. L. Bahers, P. Sautet, S. N. Steinmann, *Phys. Chem. Chem. Phys.* **2021**, *23*, 2853.
[36] G. Liu, P. Niu, C. Sun, S. C. Smith, Z. Chen, G. Q. (.M.) Lu, H.-M. Cheng, *J. Am. Chem. Soc.* **2010**, *132*, 11642.
[37] S. I. Khan, P. G. Edwards, H. S. Yuan, R. Bau, *J. Am. Chem. Soc.* **1985**, *107*, 1682.
[38] J. Zhang, X. Chen, K. Takanabe, K. Maeda, K. Domen, J. D. Epping, X. Fu, M. Antonietti, X. Wang, *Angew. Chem., Int. Ed.* **2010**, *49*, 441.
[39] Z. Teng, W. Cai, S. Liu, C. Wang, Q. Zhang, C. Su, T. Ohno, *Appl. Catal., B* **2020**, *271*, 118917.
[40] J. Wang, Z. Guan, J. Huang, Q. Li, J. Yang, *J. Mater. Chem. A* **2014**, *2*, 7960.
[41] X. Li, J. Zhang, Y. Huo, K. Dai, S. Li, S. Chen, *Appl. Catal., B* **2021**, *280*, 119452.
[42] Y. Zheng, Y. Jiao, Y. Zhu, L. H. Li, Y. Han, Y. Chen, A. Du, M. Jaroniec, S. Z. Qiao, *Nat. Commun.* **2014**, *5*, 3783.
[43] X. Li, R. Shen, S. Ma, X. Chen, J. Xie, *Appl. Surf. Sci.* **2018**, *430*, 53.
[44] P. Kumar, R. Boukherroub, K. Shankar, *J. Mater. Chem. A* **2018**, *6*, 12876.
[45] K. Dai, L. Lu, Q. Liu, G. Zhu, X. Wei, J. Bai, L. Xuan, H. Wang, *Dalton Trans.* **2014**, *43*, 6295.
[46] W.-J. Ong, L.-L. Tan, S.-P. Chai, S.-T. Yong, A. R. Mohamed, *Nano Energy* **2015**, *13*, 757.
[47] W.-J. Ong, L.-L. Tan, S.-P. Chai, S.-T. Yong, *Chem. Commun.* **2015**, *51*, 858.
[48] H. Begum, M. S. Ahmed, Y.-B. Kim, *Sci. Rep.* **2020**, *10*, 12431.
[49] T. Song, B. Long, S. Yin, A. Ali, G.-J. Deng, *Chem. Eng. J.* **2021**, *404*, 126455.
[50] B. Ai, X. Duan, H. Sun, X. Qiu, S. Wang, *Catal. Today* **2015**, *258*, 668.
[51] B.-W. Sun, H. Y. Yu, Y.-J. Yang, H.-J. Li, C.-Y. Zhai, D.-J. Qian, M. Chen, *Phys. Chem. Chem. Phys.* **2017**, *19*, 26072.
[52] L. Sun, T. Du, C. Hu, J. Chen, J. Lu, Z. Lu, H. Han, *ACS Sustainable Chem. Eng.* **2017**, *5*, 8693.
[53] H. Gu, T. Zhou, G. Shi, *Talanta* **2015**, *132*, 871.
[54] G. Peng, M. Volokh, J. Tzadikov, J. Sun, M. Shalom, *Adv. Energy Mater.* **2018**, *8*, 1800566.
[55] L. Seyfarth, J. Seyfarth, B. V. Lotsch, W. Schnick, J. Senker, *Phys. Chem. Chem. Phys.* **2010**, *12*, 2227.
[56] B. V. Lotsch, M. Döblinger, J. Sehnert, L. Seyfarth, J. Senker, O. Oeckler, W. Schnick, *Chem.* **2007**, *13*, 4969.
[57] F. Fina, S. K. Callear, G. M. Carins, J. T. S. Irvine, *Chem. Mater.* **2015**, *27*, 2612.
[58] H. Dai, X. Gao, E. Liu, Y. Yang, W. Hou, L. Kang, J. Fan, X. Hu, *Diamond Relat. Mater.* **2013**, *38*, 109.
[59] E. D'Anna, M. L. De Giorgi, A. Luches, M. Martino, A. Perrone, A. Zocco, *Thin Solid Films* **1999**, *347*, 72.
[60] A. Du, S. Sanvito, Z. Li, D. Wang, Y. Jiao, T. Liao, Q. Sun, Y. H. Ng, Z. Zhu, R. Amal, S. C. Smith, *J. Am. Chem. Soc.* **2012**, *134*, 4393.
[61] Y. Li, H. Zhang, P. Liu, D. Wang, Y. Li, H. Zhao, *Small* **2013**, *9*, 3336.
[62] J. Feng, L. Su, Y. Ma, C. Ren, Q. Guo, X. Chen, *Chem. Eng. J.* **2013**, *221*, 16.
[63] N. Hashim, Z. Muda, M. Zobir Hussein, I. Md Isa, A. Mohamed, A. Kamari, S. Abu Bakar, M. Mamat, A. Jaafar, *J. Mater. Environ. Sci.* **2016**, *7*, 3225.
[64] T.-F. Yeh, C.-Y. Teng, S.-J. Chen, H. Teng, *Adv. Mater.* **2014**, *26*, 3297.
[65] Y. Zheng, Y. Liu, X. Guo, W. Zhang, Y. Wang, M. Zhang, R. Li, Z. Peng, H. Xie, Y. Huang, *ACS Appl. Nano Mater.* **2020**, *3*, 7982.
[66] Q. Han, N. Chen, J. Zhang, L. Qu, *Mater. Horiz.* **2017**, *4*, 832.
[67] J. Zou, Y. Yu, K. Qiao, S. Wu, W. Yan, S. Cheng, N. Jiang, J. Wang, *J. Mater. Sci.* **2020**, *55*, 13618.
[68] L. Wang, W. Si, Y. Tong, F. Hou, D. Pergolesi, J. Hou, T. Lippert, S. X. Dou, J. Liang, *Carbon Energy* **2020**, *2*, 223.
[69] V. S. Vyas, V. W.-H. Lau, B. V. Lotsch, *Chem. Mater.* **2016**, *28*, 5191.
[70] F. K. Kessler, Y. Zheng, D. Schwarz, C. Merschjann, W. Schnick, X. Wang, M. J. Bojdys, *Nat. Rev. Mater.* **2017**, *2*, 17030.
[71] G. Liao, Y. Gong, L. Zhang, H. Gao, G.-J. Yang, B. Fang, *Energy Environ. Sci.* **2019**, *12*, 2080.
[72] G. Zhang, G. Li, Z.-A. Lan, L. Lin, A. Savateev, T. Heil, S. Zafeiratos, X. Wang, M. Antonietti, *Angew. Chem., Int. Ed.* **2017**, *56*, 13445.
[73] A. Savateev, S. Pronkin, J. D. Epping, M. G. Willinger, C. Wolff, D. Neher, M. Antonietti, D. Dontsova, *ChemCatChem* **2017**, *9*, 167.
[74] K. Schwinghammer, B. Tuffy, M. B. Mesch, E. Wirnhier, C. Martineau, F. Taulelle, W. Schnick, J. Senker, B. V. Lotsch, *Angew. Chem., Int. Ed.* **2013**, *52*, 2435.
[75] A. Savateev, B. Kurpil, A. Mishchenko, G. Zhang, M. Antonietti, *Chem. Sci.* **2018**, *9*, 3584.
[76] P. Niu, L.-C. Yin, Y.-Q. Yang, G. Liu, H.-M. Cheng, *Adv. Mater.* **2014**, *26*, 8046.